# Optimum Tire Contour Design Using Systematic STOM and Neural Network

**Jin-Rae Cho*, Hyun-Sung Jeong, Wan-Suk Yoo, Sung-Woo Shin**
*School of Mechanical Engineering, Pusan National University, Busan 609-735, Korea*

An efficient multi-objective optimization method is presented making use of neural network and a systematic satisficing trade-off method (STOM), in order to simultaneously improve both maneuverability and durability of tire. Objective functions are defined as follows : the sidewall-carcass tension distribution for the former performance while the belt-edge strain energy density for the latter. A back-propagation neural network model approximates the objective functions to reduce the total CPU time required for the sensitivity analysis using finite difference scheme. The satisficing trade-off process between the objective functions showing the remarkably conflicting trends each other is systematically carried out according to our aspiration-level adjustment procedure. The optimization procedure presented is illustrated through the optimum design simulation of a representative automobile tire. The assessment of its numerical merit as well as the optimization results is also presented.

**Key Words :** Multi-Objective Optimization, Tire Sidewall Contour, Maneuverability and Durability, Systematic STOM, Back-Propagation Neural Network, CPU Time

## 1. Introduction

As a key component of automobiles, tire is asked to meet various performances. Among them maneuverability and durability are most significant because both are directly related to the riding-comfort and safety of passengers. From the tire mechanics point of view, the former and the latter performances are respectively determined by the sidewall-carcass tension distribution and the belt-edge strain energy in tire inflated with air (Clark, 1982). Both mechanical quantities are in turn characterized by the tire sidewall contour (shape). For this reason, the tire contour design has become a crucial research issue in tire mechanics community since the advent of current radial tire in the mid 1910's (Purdy, 1963 ; Yamagishi et al., 1987).

The tire analysis provides us that most radial tires produce the peak strain-energy density at the belt edge. Therefore, the designer should relax it to improve the tire durability. On the other hand, Yamagishi et al. (1987) proposed that maneuverability could be improved by nonuniformly distributing the sidewall-carcass tension such that it reaches the maximum at the tire bead and the minimum at the tire shoulder. Thus, the sidewall-carcass tension distribution and the peak strain energy density at the belt edge should be chosen as the objective functions for both tire performances, and naturally the sidewall contour design becomes a multi-objective optimization problem. And, these two objective functions are to be discretized into several element-wise values in finite element approximation and the design variables are composed of the nodal radii of tire sidewall carcass.

However, there exist two major difficulties in the multi-objective sidewall contour optimization

* Corresponding Author,
**E-mail** : jrcho@pusan.ac.kr
**TEL** : +82-51-510-2467; **FAX** : +82-51-514-7640
School of Mechanical Engineering, Pusan National University, Busan 609-735, Korea. (Manuscript **Received** October 1, 2003 ; **Revised** May 11, 2004)

by traditional techniques, the strong conflicting trend between objective functions to the design variable variation and the long CPU time for the sensitivity analysis. Form our previous work (Cho et al., 2002), we observed that bead-, shoulder-side tensions and strain energy density are in the quite contrary relation to the design variables. The second difficulty is stemmed from that usual analytic or semi-analytic sensitivity scheme is not easy to apply when one uses commercial FEM code like ABAQUS because stiffness matrix is not accessible. These difficulties in the numerical optimization could be resolved by making use of neural network and interactive multi-objective optimization method (Sawaragi et al., 1985).

For the study, a back-propagation neural network model (Fausett, 1994) is used to approximate the objective functions, and its learning is performed with the help of the orthogonal array DOE (design of experiments) table (Ross, 1988). Once a neural network model is learned, the multi-objective sidewall contour optimization is performed. The constrained optimization problem is formulated according to the augmented Lagrange multiplier method (ALM) (Vanderplaats, 1984), while the sensitivity analysis is carried out by the finite difference scheme incorporated with golden section and polynomial interpolation methods. The interactive decision making during the multi-objective optimization process is performed by the effective satisficing trade-off method (STOM) (Cho et al., 2002) in which aspiration levels are systematically adjusted.

Through the optimum design simulation of a representative automobile tire, the proposed multi-objective optimization procedure is illustrated. The neural network model is assessed by comparing the optimum results and computation time with those obtained without using neural network.

## 2. Problem Description and Numerical Formulation

### 2.1 Problem description

Radial tire is in a complex structure of various rubbers, polyester and steel cords, and it may be

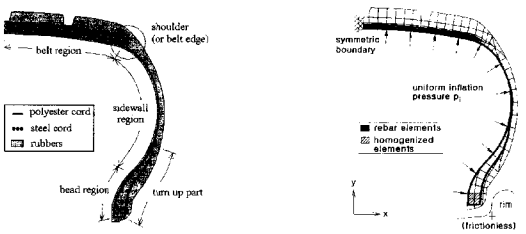


**Fig. 1** Radial automobile tire : (a) schematic section view ; and (b) 2-D FEM analysis model

refered to a book by Clark (1982) for the details of its structure and the roles of its components. As shown in Fig. 1(a), the tire carcass consisted of polyester cords is extended over belt, sidewall, bead and turn up regions, and polyester and steel cords (in the belt and bead regions) are imbedded into underlying rubbers respectively.

Since the design goal is restricted to the sidewall contour the finite element analysis and design becomes a static problem of tire inflation. Figure 1(b) shows a two-dimensional finite element model generated by I-DEAS solid modeler (2002), where the ABAQUS planar axisymmetric elements (CAX3 and CAX4 (1998)) are used. As well described in a paper by Chang et al. (1988), the planar axisymmetric model is an approximate one because an axisymmetric twist caused by the belt cord inclination to the tire meridian axis is not taken into consideration. Even though such an axisymmetric twist could be modeled with the ABAQUS generalized axisymmetric elements with twist (CGAX3 and CGAX4), one can not specify any suitable symmetric boundary condition to a half tire model shown in Fig. 1(b).

Furthermore, polyester cord and steel cords in belt layers imbedded in underlying rubbers are modeled with the ABAQUS rebar elements (1998), meanwhile bead steel cords and underlying rubber as several homogenization elements. On the other hand, the frictionless contact boundary condition is imposed to the bead-rim interface. The ABAQUS Mooney-Rivlin material model is applyed for rubber elements and the hyperelastic material model for belt and bead steel cords.

Referring to Fig. 2, there is defineed the side-

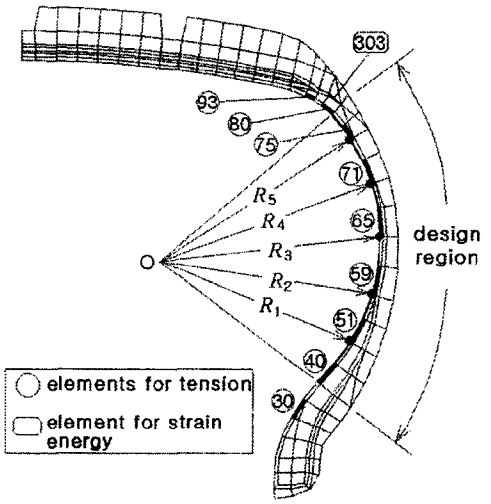


**Fig. 2** Design region and design parameters

wall carcass portion as the design region, from which some of inside nodal radii $R_i$ of carcass elements are taken as the design variable vector $X$:

$$X=\{X_1, X_2, ..., X_N\},\ X_i=R_i \tag{1}$$

By selecting some of inside carcass nodal radii, we interpolate the entire inside sidewall contour as

$$R(\theta)=\sum_{k=1}^{N} R_i\phi_i(\theta) \tag{2}$$

with Lagrange basis functions $\{\phi_i(\theta)\}$, in order to update the sidewall contour after each optimum design iteration. Mixed-type objective functions are composed of element-averaged tension values of $t$ carcass elements and strain-energy densities of $s$ belt-edge elements:

$$F(X)=\{f_1(X), f_2(X), ..., f_t(X), f_{t+1}(X), ..., f_{t+s}(X)\} \tag{3}$$

It is noted that the objective elements may be either inside the design region or not. Furthermore, some bead-side element-averaged tensions to be increased should be changed to negative values for the minimization problem. This vector-type multi-objective function is converted to a scalar-type objective function such that

$$F(X)=\max_{1\le i\le t+s}\{w_i|f_i^*-f_i(X)|\} \tag{4}$$

where, $w_i$ and $f_i^*$ denote the weighting factor and the ideal level for $i$th objective function. The ideal level means the possible peak level to which the corresponding objective function can reach ideally.

On the other hand, the tire contour design is confined with inherent constraints associated with the automobile specification and the manufacturing limitation. In the current sidewall contour design, the constraints are imposed on arc length and radius changes. By denoting $\vartheta$ be the allowable relative tolerance in the sidewall carcass arc length change and $R_i^U$, $R_i^L$ be the allowabl e upper and lower limits of the $i$ the nodal radius, the constraints are as follows:

$$(1-\vartheta)L_0\le\sum_{k=1}^{M-1}\sqrt{(x_{i+1}-x_i)^2+(y_{i+1}-y_i)^2}\le(1+\vartheta)L_0 \tag{5}$$

$$R_i^L\le R_i\le R_i^U,\ i=1, 2, ..., N \tag{6}$$

where $M$ indicates the total inside node number of carcass elements inside the design region. Even though there are constrained only the nodal radii selected for the design variables, all nodal radii within the design region satisfy the upper and lower limits due to the linear Lagrange interpolation feature. In summary, there are $N$ design variables, $(t+s)$ objective functions, and $2(N+1)$ constraints.

### 2.2 Multi-objective optimization formulation

As multi-objective sidewall contour optimization for maximizing maneuverability and durability is formulated as follows:

Find $X=\{X_1, X_2, ..., X_N\},\ X_i=R_i$ (7)

Minimize $F(X)$ (8)

Subject to $[K]\{u\}=\{f\}$ (9)

$$g_1(X)=\sum_{k=1}^{M-1}\sqrt{(x_{i+1}-x_i)^2+(y_{i+1}-y_i)^2}-(1+\vartheta)L_0\le 0 \tag{10}$$

$$g_2(X)=(1-\vartheta)L_0-\sum_{k=1}^{M-1}\sqrt{(x_{i+1}-x_i)^2+(y_{i+1}-y_i)^2}\le 0 \tag{11}$$

$$g_{i+2}(X)=R_i^L-R_i\le 0,\ i=1, 2, ..., N \tag{12}$$

$$g_{i+2+N}(X)=R_i-R_i^U\le 0,\ i=1, 2, ..., N \tag{13}$$

According to the augmented Lagrange multiplier method (ALM) (Vanderplaats, 1984), the weighted objective function subject to the inequality constraints is converted to an unconstrained pseudo-objective function given by

$$A(X;\lambda_i, \gamma_p, \psi_i)=F(X)+\sum_{i=1}^{2(N+1)}\{\lambda_i\psi_i+\gamma_p(\psi_i)^2\} \tag{14}$$

where $\lambda_i$ indicates the Lagrange multipliers, $\gamma_p$ the penalty parameter, and $\psi_i$ the constraint-dependent parameters defined later. And, the normalization factors $c_i$ between the objective functions and the constraints are defined by

$$c_i=|\nabla F(X)|/|\nabla g_i(X)| \tag{15}$$

Finally, the sidewall contour optimization problem ends up with

$$\begin{aligned}&\text{Find } X=\{X_1, X_2, \ldots, X_N\}\\ &\text{minimizing } A(X;\lambda_i, \gamma_p, \psi_i)\end{aligned} \tag{16}$$

## 3. Systematic Satisficing Trade-Off Method

### 3.1 Satisficing trade-off method (STOM) and sensitivity analysis

In usual multi-objective optimization problems, improvement of one performance may frequently degrade other performances. This conflicting trend with respect to the design variable leads to the failure in seeking a global optimum solution by usual non-interactive mathematical programming in which the designer's decision-making is not included. This implies that the designer has to interactively judge which performance should be sacrificed or improved by controlling the weights. A representative interactive multi-objective optimization method is satisficing trade-off method (STOM) introduced by Nakayama and Furukawa. (1985), in which the trade-off is accomplished by adjusting the aspiration levels $\hat{f}_i$ of individual objective functions $f_i$. Here, the aspiration level is defined as the level desired to be reached from the current level $\bar{f}_i$ of objective functions.

In the employment of STOM, the designer is asked to adjust individual aspiration levels at each trade-off iteration stage. But, without any suitable adjustment algorithm this decision-making process becomes not only painstaking but also trial and error relying on the designer's empirical know-how. In order for the systematic trade-off, this study employs the aspiration-level adjustment procedure proposed in the previous work (Cho et al., 2002), and summarizes it in the next section. Here, this study describes the sidewall contour optimization process composed of two iteration loops, the outer trade-off iteration and the inner minimization iteration.

(*Step 1*) Determine the ideal levels $f_i^*$ of individual objective functions by single-objective optimization method:

$$\boldsymbol{F}^*=\{f_1^*, f_2^*, f_3^*, \ldots, f_{t+s}^*\} \tag{17}$$

(*Step 2*) Begin the trade-off iteration ($k=1, 2, 3, \ldots$) by making initialization: $\boldsymbol{X}_k^0$, $\lambda_i^1$ and $\gamma_p^1$, and setting (or modifying) the aspiration levels $\hat{f}_i^k$ according to the systematic aspiration-level adjustment procedure,

$$\hat{\boldsymbol{F}}^k=\{\hat{f}_1^k, \hat{f}_2^k, \hat{f}_3^k, \ldots, \hat{f}_{t+s}^k\} \tag{18}$$

It is worth to note, while being updated during the minimization iteration, that each trade-off loop begins with the same initial values for parameters $\lambda_i$ and $\gamma_p$. Next, we compute the weights $w_i^k$ and the normalization factors $c_i^k$:

$$1/w_i^k=|f_i^*-\hat{f}_i^k| \tag{19}$$

$$c_i^k=|F(X_k^0+\delta X)-F(X_k^0)|/|g_i(X_k^0-\delta X)-g_i(X_k^0)| \tag{20}$$

(*Step 3*) Begin the inner loop ($l=1, 2, 3, \ldots$) for minimizing the pseudo-objective function to seek the $k$th optimum solution $\boldsymbol{X}_k$:

$$A(\boldsymbol{X}_k^l;\lambda_i^l, \gamma_p^l, \psi_i^l)=F(\boldsymbol{X}_k^l)+\sum_{i=1}^{2(N+1)}\{\lambda_i^l\psi_i^l+\gamma_p^l(\psi_i^l)^2\},$$
$$\psi_i^l=max\left[c_i^k g_i(\boldsymbol{X}_k^{l-1}), -\frac{\lambda^l}{2\gamma_p^l}\right] \tag{21}$$

During the iteration process, we evaluate the direction vector $\boldsymbol{S}^l=\{S_1^l, S_2^l, S_3^l, \ldots, S_{t+s}^l\}$ by finite difference scheme and update:

$$S_i^l=\frac{A(\boldsymbol{X}_k^{l-1}+\delta X_i;\lambda_i^l, \gamma_p^l, \psi_i^l)-A(\boldsymbol{X}_k^{l-1};\lambda_i^l, \gamma_p^l, \psi_i^l)}{\delta X_i} \tag{22}$$

$$\boldsymbol{X}_k^l=\boldsymbol{X}_k^{l-1}+\Delta\boldsymbol{X}^l,\ \Delta\boldsymbol{X}_k^l=\alpha^l\boldsymbol{S}^l \tag{23}$$

The direction vector magnitude $\alpha^l$ in Eq. (23) is determined by golden section and polynomial interpolation methods. When either of the following two convergence tolerances defined by

$$\max_{1\le i\le t+s}|\lambda_i^l-\lambda_i^{l-1}|\le\varepsilon_\lambda,\ |F(X_k^l)-F(X_k^{l-1})|/|F(X_k^l)|\le\varepsilon_F \tag{24}$$

is satisfied, we terminate the minimization iteration. Otherwise, we repeat the minimization iteration with updating

$$\lambda_i^{l+1}=\lambda_i^l+2\gamma_p^l\psi_i^l \tag{25}$$

$$\gamma_p^{l+1}=\tau\gamma_p^l \tag{26}$$

where $\tau(\tau>1)$ is an update constant.

(*Step 4*) Judge whether the optimum solution is satisfactory or not. When further trade-off is needed, go to Step 2 by letting $X_k^l$ be $X_{k+1}^0$. A judgement criterion is also summarized in the next section.

### 3.2 Systematic aspiration-level adjustment procedure

The study defines the aspiration-level indicators $\eta_i^k$ of individual objective functions, after the $k$ the trade-off iteration, by

$$\eta_i^k=|f_i^*-\bar{f}_i^k|/|f_i^*-\hat{f}_i^k|,\ i=1, 2, ..., (t+s) \tag{27}$$

where $\bar{f}_i^k$ are individual objective-function values optimized after $k$ th trade-off iteration. Then, by comparing with the preset aspiration levels $\hat{f}_i^k$, $\bar{f}_i^k$ are classified according to $\eta_i^k$ :

$$\bar{f}_i^k \Rightarrow \begin{cases} \text{exceeded } \hat{f}_i^k, & \eta_i^k<1 \\ \text{identical to } \hat{f}_i^k, & \eta_i^k=1 \\ \text{not reached to } \hat{f}_i^k, & \eta_i^k>1 \end{cases} \tag{28}$$

The choice of initial aspiration levels is rather arbitrary, but those should be located between the ideal levels and the initial objective function values. After the first trade-off iteration (i. e. $k=1$) we evaluate $\eta_i^1$, upon which we make a decision to classify individual objective functions into three sets, (i) objective functions that should be improved more ($\Im_I$), (ii) those that can be relaxed ($\Im_R$) and (iii) those that are acceptable ($\Im_A$). For the objective functions with $\eta_i^1\geq 1$ in the set $\Im_I$ and with $\eta_i^1\leq 1$ in the set $\Im_R$, as well as the whole objective functions in the set $\Im_A$, we keep the current aspiration levels for the next trade-off iteration. While, for those with $\eta_i^1<1$ in the set $\Im_I$ and with $\eta_i^1>1$ in the set $\Im_R$, aspiration levels for the next iteration are modified such that

$$|f_i^*-\bar{f}_i^1|/|f_i^*-\hat{f}_i^2|=1 \tag{29}$$

In this manner, aspiration levels are continuously adjusted, along the trade-off iteration, until all objective functions are judged to be acceptable.

According to this adjustment procedure, all aspiration-level indicators sequentially approach unity with the trade-off iteration. When all of aspiration levels are judged to be sufficiently and uniformly approached unity, we terminate the satisficing trade-off design process.

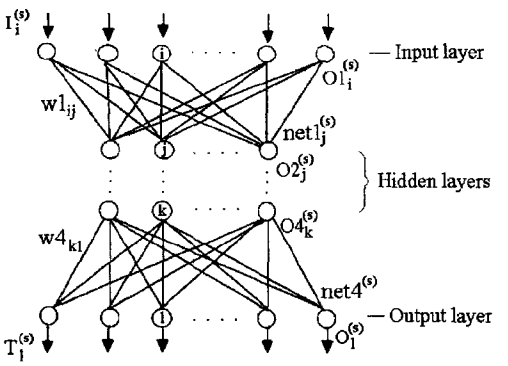


**Fig. 3** Architecture of neural network model

## 4. Approximation of Objective Function

In order to reduce the total CPU time for a large number of sensitivity analyses, we approximate (or learn) the $(t+s)$ objective functions according to a neural network model. Referring to Fig. 3, input and output layers are composed of $N$ and $M$ neurons, respectively, where $N$ is identical to the design variable number while $M$ to the objective function number $(t+s)$. On the other hand, all three hidden layers are composed of the same number of neurons as for the output layer, but the choice of neuron number for hidden layers is rather flexible. The outputs $Ol_i$ of individual neurons in the input layer are delivered to all neurons in the first hidden layer with the connecting weights $wl_{ij}$. In this manner, output signals of neurons in the upper layer are input to all neurons in the next layer with different connecting weights, up to the final output layer. Output signal from a specific neuron is made by the sigmoid transfer function to which a linear combination of weighted upper-layer output signals is input. Learning of a neural network model is performed iteratively through a series of forward computing and backward learning.

### 4.1 Forward computing

In order to learn a neural network model, we

first prepare an input data group $\boldsymbol{I}=\{\boldsymbol{I}^{(1)}, \ldots, \boldsymbol{I}^{(s)}, \ldots, \boldsymbol{I}^{(l)}\}$, $\boldsymbol{I}^{(s)}=\{I_1^{(s)}, \ldots, I_i^{(s)}, \ldots, I_N^{(s)}\}$ for the input layer and a target output data group $\boldsymbol{T}=\{\boldsymbol{T}^{(1)}, \ldots, \boldsymbol{T}^{(s)}, \ldots, \boldsymbol{T}^{(l)}\}$, $\boldsymbol{T}^{(s)}=\{T_1^{(s)}, \ldots, T_l^{(s)}, \ldots, T_M^{(s)}\}$. Both data groups contain $l$ data sets $\boldsymbol{I}^{(l)}$ and $\boldsymbol{T}^{(l)}$, respectively, where $l$ indicates the number of learning cases in DOE table. Referring to Fig. 3, each input data set $\boldsymbol{I}^{(s)}$ is composed of $N$ input data for $N$ neurons in the input layer that are chosen according to the three-level DOE table made by the orthogonal array design (Ross, 1988). Meanwhile, each target output data set $\boldsymbol{T}^{(s)}$ contains $M$ target output data for $M$ objective functions (i. e. $M$ neurons in the output layer), and those are obtained by the direct ABAQUS(1998) analysis with the corresponding input data set $\boldsymbol{I}^{(s)}$.

Besides, we set the initial connecting weights $w1_{ij}^{[1]}$, $w2_{jh}^{[1]}$, $w3_{hk}^{[1]}$ and $w4_{kl}^{[1]}$, according to the random number generation algorithm, which are double-precision real numbers within $[-0.5, 0.5]$. With the preset connecting weights, we perform initial forward computations for $l$ learning cases. Let us describe the forward computing process for a specific learning case $s$.

Individual input-layer neurons generate output signals given by

$$O1_i^{(s)}=I_i^{(s)},\ i=1, 2, \ldots, N,\ s=1, 2, \ldots, l \quad (30)$$

and which transfer to all neurons in the first hidden layer. Then, each neuron in the first hidden layer produces output signal $O2_j^{(s)}$ through the transfer function processing of a linear combination of the connecting weights $w1_{ij}^{[1]}$ and the input signals $O1_i^{(s)}$:

$$O2_j^{(s)}=f(net1_j^{(s)}),\ net1_j^{(s)}=\sum_{i=1}^{N} w1_{ij}^{[1]} O1_i^{(s)} \quad (31)$$

where, $f(\cdot)$ is the sigmoid function defined by $f(x)=1/(1+e^{-x})$.

In this manner, the other two hidden layers generate output signals $O3_h^{(s)}$ and $O4_k^{(s)}$, respectively. Passing through the output layer provides us an output set corresponding to the learning case $s$ such that

$$O_l^{(s)}=f(net4_l^{(s)}),\ net4_l^{(s)}=\sum_{k=1}^{M} w4_{kl}^{[1]} O4_k^{(s)} \quad (32)$$

After completing the forward computing for all learning cases with the preset connecting weights, we have an initial output data group given by

$$\boldsymbol{O}=\{\boldsymbol{O}^{(1)}, \ldots, \boldsymbol{O}^{(s)}, \ldots, \boldsymbol{O}^{(l)}\},\ \boldsymbol{O}^{(s)}=\{O_1^{(s)}, \ldots, O_i^{(s)}, \ldots, O_M^{(s)}\} \quad (33)$$

It is worth to mention that we normalize target output data $\boldsymbol{T}^{(s)}$ because the sigmoid function produces signals between 0 and 1.

### 4.2 Backward learning

Following the forward computing, we perform the backward learning for adjusting the initial connecting weights, in order to reduce the learning error of the neural network model defined by

$$E^{(s)}=\frac{1}{2}\sum_{l=1}^{M}(T_l^{(s)}-O_l^{(s)})^2 \quad (34)$$

It is worth to note that the backward learning is also preformed separately for different learning cases. But, differing from the forward computing, the connecting weight adjustment is carried out in the reverse direction. In other words, the connecting weights $w4_{kl}$ between the output and the third layers are updated first, and so forth.

According to usual minimization principle, the variations of connecting weights between arbitrary two layers are calculated by

$$\Delta wI_{kl}^{(s)}=-\eta\frac{\partial E^{(s)}}{\partial wI_{kl}},\ I=1, 2, 3, 4 \quad (35)$$

where $\eta\,(\eta<1)$ is defined by the preset learning ratio. For the connecting weights between output and the third hidden layers, we use the following chain rule together with $e^{-net4_l^{(s)}}=(1-O_l^{(s)})/O_l^{(s)}$ derived from Eqs. (31) and (32):

$$\begin{aligned}\frac{\partial E^{(s)}}{\partial w4_{kl}}&=\frac{\partial E^{(s)}}{\partial O_l^{(s)}}\frac{\partial O_l^{(s)}}{\partial net4_m^{(s)}}\frac{\partial net4_m^{(s)}}{\partial w4_{kl}}\\&=-(T_l^{(s)}-O_l^{(s)})\,O_l^{(s)}(1-O_l^{(s)})\,O4_k^{(s)}\end{aligned} \quad (36)$$

Substituting Eq. (36) into Eq. (35) leads to

$$\Delta w4_{kl}^{(s)}=\eta\delta4_l^{(s)}O4_k^{(s)},\ \delta4_l^{(s)}=(T_l^{(s)}-O_l^{(s)})\,O_l^{(s)}(1-O_l^{(s)}) \quad (37)$$

For the connecting weights between last two hidden layers, we apply one more chain rule to the first term on the right-hand-side of Eq. (36) such that

$$\frac{\partial E^{(s)}}{\partial w3_{hk}}=\frac{\partial E^{(s)}}{\partial O4_i^{(s)}}\frac{\partial O4_i^{(s)}}{\partial net3_n^{(s)}}\frac{\partial net3_n^{(s)}}{\partial w3_{hk}}$$
$$=\left[\frac{\partial E^{(s)}}{\partial net4_i^{(s)}}\frac{\partial net4_i^{(s)}}{\partial O4_i^{(s)}}\right]\frac{\partial O4_i^{(s)}}{\partial net3_m^{(s)}}\frac{\partial net3_m^{(s)}}{\partial w3_{hk}} \quad (38)$$

Then, this relation leads

$$\Delta w3_{hk}^{(s)}=\eta\delta3_k^{(s)}O3_h^{(s)}=\left(\sum_{i=1}^{M}\delta4_i^{(s)}w4_{ki}^{[1]}\right)O4_k^{(s)}(1-O4_k^{(s)}) \quad (39)$$

Along the similar procedure, it is not hard to derive the next two relations for the remaining connecting weights :

$$\Delta w2_{jh}^{(s)}=\eta\delta2_h^{(s)}O2_j^{(s)},\ \delta2_h^{(s)}=\left(\sum_{k=1}^{M}\delta3_k^{(s)}w3_{hk}^{[1]}\right)O3_h^{(s)}(1-O3_h^{(s)}) \quad (40)$$

$$\Delta w1_{ij}^{(s)}=\eta\delta1_j^{(s)}O1_i^{(s)},\ \delta1_j^{(s)}=\left(\sum_{h=1}^{M}\delta2_h^{(s)}w2_{jh}^{[1]}\right)O2_j^{(s)}(1-O2_j^{(s)}) \quad (41)$$

After completing backward learning for all learning cases, we modify the current connecting weights such that

$$wI_{ij}^{[p+1]}=wI_{ij}^{[p]}+\frac{1}{l}\sum_{s=1}^{l}\Delta wI_{ij}^{(s)},\ I=1,\ 2,\ 3,\ 4 \quad (42)$$

for the next forward computing. A series of forward computing and backward learning repeats until the output-layer signals satisfy the stop criterion defined by $\max_{1\le i\le M,1\le s\le l}|O_i^{(s)}-T_i^{(s)}|\le\varepsilon_T$.

## 5. Numerical Experiments

According to the theoretical formulations we develop a test optimization program, and which is interfaced with I-DEAS(2002) and ABAQUS (1998) commercial codes. A representative P205/65R14 automobile tire is considered, and its 2-D FEM mesh and the problem definition are depicted in Figs. 1(b) and 2, respectively. Five nodal radii of inner carcass elements are defined as the design variables, while nine carcass-elements and one belt-edge element are taken for element-averaged carcass tensions and strain-energy intensity, respectively (element numbers are labeled in Fig. 2). Simulation data for the neural network learning and the contour optimization are given in Table 1, and the initial radii $R_i$ of five design variables are equally 2.075*in*. By taking the initial radii as the design variable values for level 1, the other two levels are selected by applying increments to the initial radii : $R_i=(2.075-0.1)$ *in* for level 2 and $R_i=(2.075+0.1)$ *in* for level 3.

**Table 1** Data taken for numerical simulation

| Parameters | Values |
|---|---|
| *For neural network learning* | |
| Type of DOE table | $L_{27}(3^{13})$ |
| Number of design variable levels | 3 |
| Design variable variations for three levels | $0in, \pm0.1in$ |
| Number of neurons in input layer | 5 |
| Neuron numbers in hidden and output layers | 10, 10 |
| Learning ratio and learning tolerance $\eta$, $\varepsilon_T$ | 0.8, 0.005 |
| *For numerical optimization* | |
| Design variable number $N$ | 5 |
| Numbers of objective functions $f_t$, $f_s$ | 9, 1 |
| Allowable tolerance of arc length change $\vartheta$ | 0.1(10%) |
| Allowable nodal radius change $\delta R_i$ | $\pm0.2in$ |
| Initial Lagrange multiplier $\lambda_i^0$ | 0 |
| Initial penalty parameter and $\gamma_p^0$ | 1 |
| Update constant $\tau$ | 10 |

We first learned the back-propagation neural network model with three hidden layers according to the learning procedure described in Section 4. After that, we set the ideal levels for ten objective functions with the help of SOP (single-objective optimization). As well, we set the first aspiration levels based on the initial objective functions and the ideal levels. Those levels selected are given in Fig. 4 and Table 2. We note that all numerical data are obtained using the neural network model.

Referring to Fig. 4, seven of the SOP values are directly taken as ideal levels, but two of the SOP values are modified for the ideal levels of $f_3$ and $f_5$. The SOP value of $f_3$ is higher than two bead-side ideal levels so that it was modified. Meanwhile, The SOP value of $f_5$ obtained by the tension minimization is not appropriate for the ideal level, because its position, from which the SOP switched to the minimization problem from the maximization one, is rather ambiguous weather the carcass tension should be increased or decreased. For this reason, we adjust it by moving it towards the initial value. Meanwhile, initial aspiration levels $\hat{f}_i^1$ are set by shifting the initial values towards the ideal levels such that those are located between the ideal and initial levels.

With the initial aspiration levels $\hat{f}_i^1$ we begin

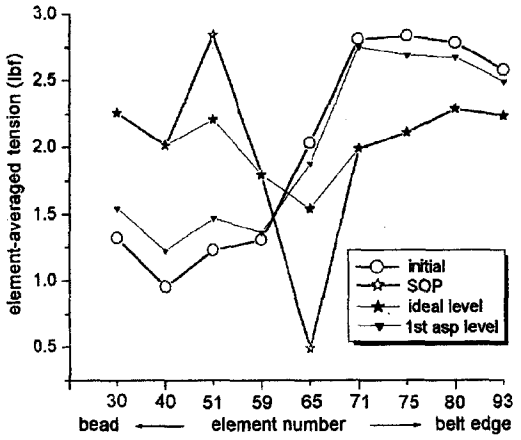


**Fig. 4** Ideal levels and first aspiration levels

the interactive trade-off iteration. The first optimum solutions $\bar{f}_i^1$ and the corresponding aspiration-level indicators $\eta_i^1$ evaluated according to Eq. (27) are recorded in Table 2. The tension values $\bar{f}_1^1 \sim \bar{f}_3^1$ of three bead-side elements and the belt-edge strain energy intensity $\bar{f}_{10}^1$ are shown improved slightly, so we classify these four functions into the set $\Im_I$ for further improvement. On the other hand, the other six become worse on the whole than the initial values. Because of the great importance of the belt-edge carcass tension for the maneuverability improvement, we classify two belt-edge-side tensions $f_8 - f_9$ into the set $\Im_I$. Meanwhile, the tension values $f_4 \sim f_7$ are of middle carcass elements, so the improvement direction in such tension values is rather ambiguous at the initial design stage. From this reason, we keep the current levels $\bar{f}_5^1 - \bar{f}_6^1$ of two center elements (by classifying into the set $\Im_A$) and sacrifice the other two by classifying into the set $\Im_R$.

According to the aspiration-level adjustment

**Table 2** Iteration-wise optimization results according to the neural network and systematic satisficing trade-off method (unit of strain energy intensity : $lbf \cdot in/in^2$)

| Element-averaged | Carcass tension | | | | | | | | | Strain energy intensity |
|---|---|---|---|---|---|---|---|---|---|---|
| Objective function | $f_1(30)$ | $f_2(40)$ | $f_3(51)$ | $f_4(59)$ | $f_5(65)$ | $f_6(71)$ | $f_7(75)$ | $f_8(80)$ | $f_9(93)$ | $f_{10}(303)$ |
| *Ideal level* $f_i^*$ | 2.263 | 2.014 | 2.211 | 1.793 | 1.543 | 1.988 | 2.113 | 2.292 | 2.238 | 2.090 |
| *Initial level* $f_{i,N}^0$ | **1.326** | **0.940** | **1.225** | **1.323** | **2.035** | **2.819** | **2.847** | **2.787** | **2.575** | **2.580** |
| Asp. level 1 $\hat{f}_i^1$ | 1.546 | 1.223 | 1.471 | 1.359 | 1.878 | 2.754 | 2.689 | 2.675 | 2.491 | 2.300 |
| *Optimum 1* $\bar{f}_i^1$ | 1.485 | 1.074 | 1.248 | 1.269 | 1.835 | 2.847 | 2.898 | 2.808 | 2.583 | 2.373 |
| Indicator 1 $\eta_i^1$ | 1.086 | 1.187 | 1.300 | 1.208 | 0.872 | 1.361 | 1.346 | 1.362 | 1.302 | 1.349 |
| Decision 1 | I | I | I | R | A | A | R | I | I | I |
| Asp. level 2 $\hat{f}_i^2$ | 1.546 | 1.223 | 1.471 | 1.269 | 1.878 | 2.754 | 2.893 | 2.675 | 2.491 | 2.300 |
| *Optimum 2* $\bar{f}_i^2$ | 1.805 | 1.445 | 1.605 | 1.208 | 1.743 | 2.787 | 3.012 | 2.715 | 2.510 | 2.277 |
| Indicator 2 $\eta_i^2$ | 0.639 | 0.719 | 0.819 | 1.116 | 0.598 | 1.043 | 1.145 | 1.104 | 1.075 | 0.893 |
| Decision 2 | I | I | I | R | A | R | R | I | I | I |
| Asp. level 3 $\hat{f}_i^3$ | 1.805 | 1.445 | 1.605 | 1.208 | 1.878 | 2.787 | 3.012 | 2.675 | 2.491 | 2.277 |
| *Optimum 3* $\bar{f}_i^3$ | 1.814 | 1.448 | 1.596 | 1.202 | 1.730 | 2.797 | 3.008 | 2.693 | 2.495 | 2.286 |
| Indicator 3 $\eta_i^3$ | 0.979 | 0.994 | 1.014 | 1.009 | 0.558 | 0.995 | 0.995 | 1.047 | 1.013 | 1.047 |
| Decision 3 | I | I | A | A | I | A | A | I | A | R |
| Asp. level 4 $\hat{f}_i^4$ | 1.814 | 1.448 | 1.605 | 1.208 | 1.730 | 2.787 | 3.012 | 2.675 | 2.491 | 2.286 |
| *Optimum 4* $\bar{f}_i^4$ | 1.816 | 1.454 | 1.616 | 1.200 | 1.613 | 2.799 | 3.009 | 2.681 | 2.485 | 2.279 |
| Indicator 4 $\eta_i^4$ | 0.994 | 0.989 | 0.980 | 1.013 | 0.374 | 1.014 | 0.996 | 1.014 | 0.975 | 0.961 |
| Decision 4 | A | A | A | A | I | R | A | A | A | A |
| Asp. level 5 $\hat{f}_i^5$ | 1.814 | 1.448 | 1.605 | 1.208 | 1.613 | 2.799 | 3.011 | 2.675 | 2.491 | 2.286 |
| *Optimum 5* $\bar{f}_i^5$ | 1.822 | 1.452 | 1.601 | 1.201 | 1.610 | 2.794 | 3.008 | 2.664 | 2.473 | 2.284 |
| Indicator 5 $\eta_i^5$ | 0.982 | 0.993 | 1.005 | 1.011 | 0.995 | 0.993 | 0.996 | 0.971 | 0.928 | 0.989 |
| Decision 5 | A | A | A | A | A | A | A | A | A | A |

**Table 3 Comparison of multi-objective optimization results between neural network expectation and ABAQUS analysis (unit of strain energy intensity: $lbf \cdot in/in^2$)**

| Element-averaged | Carcass tension ($lbf$) | | | | | | | | | Energy Intensity |
|---|---|---|---|---|---|---|---|---|---|---|
| Objective function | $f_1(30)$ | $f_2(40)$ | $f_3(51)$ | $f_4(59)$ | $f_5(65)$ | $f_6(71)$ | $f_7(75)$ | $f_8(80)$ | $f_9(93)$ | $f_{10}(303)$ |
| Initial value $f_{i,N}^0$ | 1.326 | 0.940 | 1.225 | 1.323 | 2.035 | 2.819 | 2.847 | 2.787 | 2.575 | 2.580 |
| MOP value $\bar{f}_{i,A}$ | 1.811 | 1.458 | 1.579 | 1.161 | 1.902 | 2.849 | 2.919 | 2.661 | 2.479 | 2.365 |
| MOP value $\bar{f}_{i,N}$ | 1.800 | 1.425 | 1.551 | 1.216 | 1.693 | 2.823 | 2.972 | 2.652 | 2.467 | 2.297 |
| *Difference* $\Delta_{MOP}$ | −0.006 | −0.023 | −0.018 | 0.047 | −0.110 | −0.009 | 0.018 | −0.003 | −0.005 | −0.029 |

technique described before we adjust the initial aspiration levels for the next iteration. As given in Table 2, only two of them are modified, $\hat{f}_4^2$ and $\hat{f}_7^2$ underlined. After the second iteration, three bead-side tension values $\bar{f}_1^2 \sim \bar{f}_3^2$ and belt-edge strain energy intensity $\bar{f}_{10}^2$ are shown improve d more than the desired second aspiration levels. Two belt-edge tension values $\bar{f}_8^2 - \bar{f}_9^2$ are shown lowered but not reached to the aspiration levels. Hence we make a decision to classify these six functions into the set $\Im_I$, in order for further max-in variation in the sidewall carcass tension distribution and further reduction of strain-energy intensity. On the other hand, we sacrifice the four middle tension values by classifying those into the sets $\Im_R$ and $\Im_A$, in order to increase the weights for the above-mentioned six functions relatively.

The third aspiration levels $\hat{f}_i^3$ are listed in Table 2, where three are kept unchanged according to the aspiration-level adjustment procedure, together with the corresponding optimum solutions and aspiration-level indicators. In order for further increase of the bead-side tension we classify $f_1$ and $f_2$ into the set $\Im_I$. In addition, the center tension $\bar{f}_5^3$ is judged to be relatively high so that we decide to lower it. Meanwhile, we experienced that belt-edge tension and strain-energy intensity are in conflicting relation, so we sacrifice $f_{10}$ (by classifying into the set $\Im_R$) in order for further decrease of tension value $\bar{f}_8^3$. In this manner we complete the multi-objective optimization in five iterations.

As can be realized from Table 2, all of aspiration-level indicators approach unity with the trade-off iteration, and those show a uniform distribution after the final iteration. Even though it is natural, different Pareto solutions would be reached when different combinations of trade-off decision-makings are made. However, the adjustment procedure of aspiration levels is systematically performed in terms of the aspiration-level indicators and three decision-making categories. As a result, the designer's burden in adjusting the aspiration levels becomes relaxed.

Comparison of final ten objective-functions $\bar{f}_{i,N}$ with the initial ones $f_{i,N}^0$ is made in Table 3. Three bead-side tension values are considerably increased, and two belt-edge tension values and strain-energy intensity are also remarkably decreased, which was desired for the maneuverability and durability improvement. On the other hand, two tension values, $f_4(59)$ and $f_7(75)$, are shown to be degraded compared to the initial ones, and which is of course resulted from the sacrificing of them to improve the other six functions. The comparison of sidewall carcass tension distributions between initial and optimum contours is given in Fig. 5. As well as, we record the optimum solutions $\bar{f}_{i,A}$ obtained without using neural network, for the purpose of the neural network assessment, which are of course achieved with the same ideal levels, aspiration levels and decision criterion that the case using neural network took. The relative difference $\Delta_{MOP}$ is defined by $(\bar{f}_{i,N} - \bar{f}_{i,A})/\bar{f}_{i,A}$. Both cases show a good agreement each other with the maximum relative difference less than 5%.

In Table 4, the optimum solutions of five design variables $\bar{R}_{i,N}$ are compared with the initial ones and the optimum solutions obtained without neural network. We see that all design variables satisfy the constraints imposed on the optimi-

**Table 4 Comparison of optimum nodal radii (unit: *in*)**

| | $R_1$ | $R_2$ | $R_3$ | $R_4$ | $R_5$ | $L$ |
|---|---|---|---|---|---|---|
| Initial $R_i^0$ | 2.075 | 2.075 | 2.075 | 2.075 | 2.075 | 3.238 |
| Optimum $\bar{R}_{i,A}$ | 2.036 (−0.039) | 1.965 (−0.110) | 1.998 (−0.077) | 2.055 (−0.020) | 2.139 (0.064) | 3.204 (−1.05%) |
| Optimum $\bar{R}_{i,N}$ | 2.026 (−0.049) | 1.975 (−0.100) | 1.950 (−0.125) | 2.017 (−0.058) | 2.151 (0.076) | 3.196 (−1.30%) |
| Difference $\Delta_{VAR}$ | −0.005 | 0.005 | −0.024 | −0.018 | 0.006 | −0.002 |

(*): calculation of $\delta R_i$ or $\vartheta$.

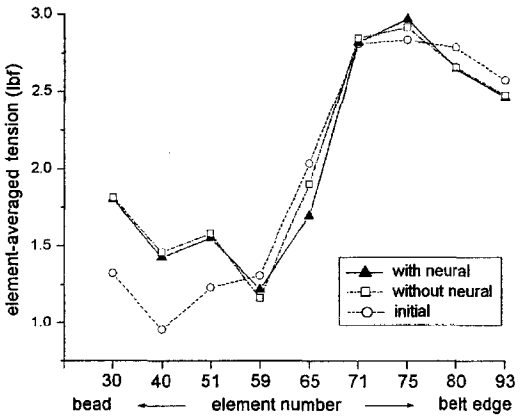


**Fig. 5** Carcass tension distribution after optimization

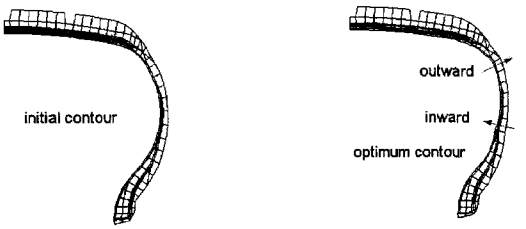


**Fig. 6** Sidewall carcass contours: (a) initial; and (b) optimum

zation problem and the relative differences $\Delta_{VAR}$ between two optimum solutions are less than 3%. Referring to Fig. 6 showing the comparison of initial and optimum sidewall contours, the initial one should be moved inward, while being moved outward at the tire shoulder region, in order to enhance both maneuverability and durability. It is worthy mentioning that the optimum contour needs to be smoothened by curve fitting with a number of polynomials. The reason is because the bumpy contour obtained by the numerical optimization not only cause difficulty in manufacturing but also produce stress concentration.

**Table 5 Total CPU time spent for optimization**

| | Optimization SOP | Optimization MOP | Neural network learning | CPU Time |
|---|---|---|---|---|
| Without neural Network | 26 hrs (390) | 10 hrs (156) | None | 36hrs |
| Neural network | 1 hr | | 8 hrs (27) | 9 hrs |

(*): FEM analysis times.

Comparison of the total CPU times spent for the sidewall are presented in Table 5, in which SOP is used only for the ideal level setting. The case with neural network requires extra time for the neural network learning, but the total CPU time is considerably reduced by four times. Fur thermore, it requires only 27 times of FEM analyses for the neural network learning. As a result, the CPU-time effectiveness of neural network is also preposterous for the interactive multi-objective optimization.

## 6. Conclusion

A systematic and time-effective multi-objective optimization procedure has been addressed in order to simultaneously improve both maneuverability and durability of automobile tires. For which a back-propagation neural network model was incorporated with our previous systematic satisficing trade-off method (STOM), together with the use of the orthogonal array DOE technique and the mathematical finite difference scheme for the sensitivity analysis. The proposed optimization procedure was applied to the sidewall contour design of a representative automobile tire model (P205/65R14), and compared

with that relying on by the FEM-based finite difference sensitivity analysis (i. e. without neural network learning). The expectation accuracy of the neural network model has been verified to be reliable from the relative difference evaluation: less than 5% in multi-objective optimum results while less than 3% in the final optimum sidewall radii. In the computation efficiency aspect, the proposed method requires FEM analyses only for the neural network learning, so that the total CPU time was reduced considerably by four times.

## Acknowledgements

Two authors (WSY and SWS) would like to thank the Ministry of Science and Technology of Korea for the financial support by a grant (M1-0203-00-0017-02J0000-00910) under the National Research Laboratory. And, the financial support for this work by R&D Center of Kumho Industrial Co., Ltd. is also gratefully acknowledged.

## References

*ABAQUS Standard User's Manual, Version 5. 8*. Hibbitt, Karlsson & Sorensen, Inc.: Pawtucket, 1998.

Chang, J. P., Satyamurthy, K. and Tseng, N. T., 1988, "An efficient approach for three dimensional finite element analysis of tires," *Tire Science and Technology TSTCA*, Vol. 16, p. 249~273.

Cho, J. R., Jeong, H. S., Kim, N. J. and Kim, K. W., 2002, "Application of STOM to the optimal tire contour Design by Introducing the Aspiration-Level Indicator," *Tire Science and Technology TSTCA*, Vol. 30, No. 4, p. 265~288.

Clark, S. K., 1982, *Mechanics of Pneumatic Tires*, Government Printing Office, Washington D. C.

Fausett, L., 1994, *Fundamentals of Neural Networks*, Prentice-Hall, New Jersey.

*I-DEAS Master Series, Release 9*, Structural Dynamics Research Corporation : Ohio, 2002.

Nakayama, H. and Furukawa, K., 1985, "Satisficing trade-off method with an application to multiobjective structural design," *Large Scale Systems*, Vol. 8, p. 47~57.

Purdy, J. F., 1963, *Mathematics Underlying Design of Pneumatic Tires*, Edwards Brothers, Michigan.

Ross, P. J., 1988, *Taguchi Techniques for Quality Engineering*, McGraw-Hill, New York.

Sawaragi, Y., Nakayama, H. and Tanino, T., 1985, *Theory of Multiobjective Optimization*, Academic Press, New York.

Vanderplaats, G. N., 1984, *Numerical Optimization Techniques for Engineering Design with Applications*, McGraw-Hill, Singapore.

Yamagishi, K., Togashi, M., Furuya, S., Tsukahara, K. and Yoshimura, N., 1987, "A Study on the Contour of the Radial Tire: rolling optimization theory (RCOT)," *Tire Science and Technology TSTCA*, Vol. 15, No. 1, p. 3~29.